micromachines

MDPI

Article

Additive Modulated Perovskite Microstructures for High Performance Photodetectors

Zhan Gao [1,2], Yifan Zheng [1], Guancheng Huang [1], Genjie Yang [1], Xinge Yu [2,*] and Junsheng Yu [1,*]

1 State Key Laboratory of Electronic Thin Films and Integrated Devices, School of Optoelectronic Science and Engineering, University of Electronic Science and Technology of China (UESTC), Chengdu 610054, China; zhangao2-c@my.cityu.edu.hk (Z.G.); yifanzheng_uestc@163.com (Y.Z.); dkdkdkdz@163.com (G.H.); genjieyang@std.uestc.edu.cn (G.Y.)

2 Department of Biomedical Engineering, City University of Hong Kong, Hong Kong 999077, China

* Correspondence: xingeyu@cityu.edu.hk (X.Y.); jsyu@uestc.edu.cn (J.Y.)

Received: 3 November 2020; Accepted: 2 December 2020; Published: 10 December 2020

Abstract: Organic-inorganic hybrid perovskites have been widely used as light sensitive components for high-efficient photodetectors due to their superior optoelectronic properties. However, the unwanted crystallographic defects of perovskites typically result in high dark current, and thus limit the performance of the device. Herein, we introduce a simple route of microstructures control in $MAPbI_3$ perovskites that associates with introducing an additive of 3,3,4,4-benzophenonetetracarboxylic dianhydridean (BPTCD) for crystallization adjustment of the perovskite film. The BPTCD additive can facilitate the formation of high-quality perovskite film with a compact and nearly pinhole-free morphology. Through characterizing the molecular interactions, it was found that the carbonyl groups in BPTCD is the key reason that promoted the nucleation and crystallization of $MAPbI_3$. As a result, we obtained high-efficient and stable perovskite photodetectors with low dark current of 9.98×10^{-8} A at −0.5 V, an on/off ratio value of 10^3, and a high detectivity exceeding 10^{12} Jones over the visible region.

Keywords: perovskite film; $MAPbI_3$ microstructure; additive modulation; photodetectors; high detectivity

1. Introduction

Recently, organic-inorganic hybrid perovskites have attracted enormous interest due to their superior optoelectronic properties, including high charge carrier mobility, long carrier diffusion length, and a broad range of bandgap [1–10]. These remarkable optoelectronic properties have provoked numerous researches on perovskite electronics, such as solar cells [1–4], light-emitting diodes [5–7], lasers [8–10] and photodetectors [11–14]. Among these devices, perovskite photodetectors (PePDs) can make instantaneously transition between optical and electrical signals, which broaden a route for many important applications including environmental monitoring, optical communication, remote control, and biological sensing [11,12]. In 2014, Hu et al. reported a wide optical range PePD for the first time, whose photo-responsivity was 3.49 A W^{-1}, 0.0367 A W^{-1} at 365 nm and 780 nm with a voltage bias of 3 V [11]. Later on, Yang et al. demonstrated a solution-processed PePD based on $MAPbI_{3-x}Cl_x$ film, with a high detectivity (D*) value of 8×10^{13} Jones at −100 mV [12]. Since then, various strategies, including tuning film quality of perovskites [14–21], device structure optimization [22–27], and introducing novel materials [28–31] have been adopted to enhance the device performance.

The performance of PePDs is strongly related to the optoelectronic properties of the perovskite film, which mainly associates with its intrinsic natures such as crystallographic defects, surface morphology, and crystalline size [32,33]. Many routes have been explored to improve the quality of perovskite film. Surface modification of perovskite films is one of the effective methods to fabricate high-qualiy perovskite film [4,13,34,35]. Zheng et al. applied poly(perfluorobutenylvinylether) to modifiy the perovskite surface, obtaining a efficient and stable perovskite solar cell [4]. Ambient Air Plasma was also studied to modify the surface of perovskite film [34]. Zhao et al. used an anti-solvent additive to improve the quality of the perovskite films [13]. The resulted perovskite films exhibit good crystallinity and uniformity, and the correponding PePDs revealed a high D* of 10^{12} and 10^{11} Jones in the Visible and near-infrared regions, respectively. Another successful example is introducing vapor-assisted process for the purpose of perovskite film modification, and the D* of the resulting PePDs could achieve 3×10^{12} Jones at −0.1 V [15]. Furthermore, the crystallization of the perovskite films can also be optimized by novel film deposition method, such as nano-imprint lithography [16,17]. Nanoscale-patterned and vertically grown halide perovskites realized by these imprinting methods improved the photo-response and performance of the PePDs significantly. Although the pattern-assisted processes can improve the quality of perovskite film obviously, the requirement of special pattern molds increases the complexity of fabrication processes. Hence, developing a concise and low-cost method for high-quality perovskite can contribute fudamental understanding of high performance PePDs.

In this work, we present a simple approach to tune the $MAPbI_3$ microstructures and improve the film quality, by introducing a crystallization controlling additive of 3,3,4,4-benzophenonetetracarboxylic dianhydridean (BPTCD). The BPTCD additive can facile the heterogeneous nucleation of the $MAPbI_3$ through the interaction between carbonyl (C=O) and PbI_2, which lowering the energy barrier of nucleation and thus significantly suppressed the dark current (I_d) in the PePDs. Based on the additive controlled high-quality perovskite film, we realized a high performance PePDs with a low I_d of 9.98×10^{-8} A at −0.5 V, a high on/off ratio of 10^3, and a D* value 10^{12} Jones over visible region.

2. Materials and Methods

The perovskite precursor solution was prepared by mixing 744 mg MAI with 254.3 mg PbI_2 (Polymer Light Technology Corp., Xi'an, China) in 1 mL DMF (Sigma-Aldrich, St. Louis, MO, USA). BPTCD was purchased from Sigma-Aldrich and used as received. Adding BPTCD into the perovskite precursor formed solution with concentrations ranging from 1 to 4 wt.%. The above solution was stirred at 60 °C overnight to ensure the adequate dissolution. The device fabrication began on an ITO coated glass substrate where thin film ITO with a sheet resistance of 15 Ω/sq acted as anodes. The substrates were cleaned in an ultrasonic bath with detergent water, acetone, deionized water, and isopropyl alcohol successively. Then the ITO glasses were nitrogen blew dry and then treated with oxygen plasma under a pressure of 25 Pa for 5 min to modify the surface energy of the ITO. PEDOT:PSS was spin-coated at 5000 rpm for 60 s and immediately annealed at 145 °C for 15 min. Then, substrates were transferred into a N_2 filled glove box. The perovskite solution was spin-coated onto the PEDOT:PSS film (2500 rpm for 40 s). 300 µL chloro-benzene (CB) was dropped onto the samples 7 s after the start of spin-coating. Samples were then annealed at 105 °C for 15 min. Afterwards, the dichlorobenzene solvent of $PC_{61}BM$ was spun at 3000 rpm for 40 s on the perovskite film and annealed at 100 °C for 20 min. Finally, the devices were completed by consecutive vacuum deposition of an Ag cathode (100 nm) under 10^{-5} mbar. The overlap between ITO and Ag electrodes was 0.02 cm^2, which is the active absorption area of the devices. For the reference n-type (electron-only) devices, the perovskite film was sandwiched in the middle of the $PC_{61}BM$ films. $PC_{61}BM$ with a concentration of 20 mg/mL was spun-coated on ITO at a rate of 2000 rpm for 60 s inside the glove box. Finally, Ag (100 nm) is thermally deposited under high-vacuum condition.For the Fourier Transform Infrared (FTIR) measurements, all samples were spin-coated on the ITO coated glass substrates at a rate of 1000 rpm for 60 s. The concentration of the precursor solution was 50 mg/mL for the pure BPTCD

sample. The precursor solution for the BPTCD:PbI_2 sample was prepared by dissolving 25 mg BPTCD and 40 mg PbI_2 in 1 mL DMF.

The current density-voltage-luminance (J-V-L) characteristics were tested in dark and under a white light (100 mW/cm^2) with a Keithley 4200 source. Quantum efficiency test system (Zolix SC 100, Beijing, China) was used to obtain the EQE spectra then detectivity was calculated based on the obtained EQE results. The absorption spectra were acquired on a Horiba 320 detector. The surface morphology and the cross-section view of the perovskite film were characterized by scanning electron microcopy (SEM, FEI Inspect F50, FEI Company, Eindhoven, The Netherlands). Surface morphologies of active layers were characterized by atomic force microscope (AFM, AFM 5500, Agilent, Tapping Mode, Chengdu, China). The crystalline structures were characterized by X-ray diffraction (XRD, D2 PHASER, Karlsruhe, Germany). The Thermo Scientific Escalab 250Xi with an ultraviolet photoelectron spectroscopy (UPS) system was used to measure the energy level of the perovskite layers. Fourier-transform infrared (FTIR) measurement was conducted with a FTIR spectrometer (Thermo Cientific, Nicole−10, Waltham, MA, USA). The impedance spectra were measured by Agilent precision impedance analyzer 4294A. All the measurements were performed in air at room temperature without encapsulation.

3. Results

Figure 1a shows the explored view of the schematic diagram for the PePDs in this work, with the multiple layers structure of indium tin oxide (ITO)/poly(3,4-ethylenedioxythiophene):polystyrene sulfonate (PEDOT:PSS) (40 nm)/$MAPbI_3$:BPTCD (~400 nm)/$PC_{61}BM$ (70 nm)/Ag (~100 nm). To investigate the photo responsivity of the perovskite film, we firstly measured the UV-Visible absorption spectra of the perovskite films with and without BTPCD. As shown in Figure 1b, the absorption spectra of these two films are almost overlap, indicating that BPTCD additive doesn't change the visible light absorption properties of the perovskite film. Microstructures of the $MAPbI_3$ were then characterized by XRD measurement and summarized in Figure 1c. The XRD patterns show three main diffraction peaks at 14.3°, 28.6° and 32.2° for all perovskite films, which represent the (110), (220) and (310) planes, respectively. The other weak diffraction peaks appear at 19.9°, 23.3°, 24.5°, 40.5°, 43.1° and 50.2° represent crystal indices (112), (211), (202), (224), (314) and (404) of the perovskites. All the diffraction peaks are in good agreement with literature reports [12,13,36]. Such results indicate that the orthorhombic crystal structure exists in both pure perovskite and the BPTCD added perovskite films [37]. However, the intense diffraction peaks of the BPTCD added perovskite film demonstrate greater crystallinity. We note here that the enhancements of crystallinity are favorable to reduce the traps, suppress the recombination of charge carries and consequently lower the dark current.

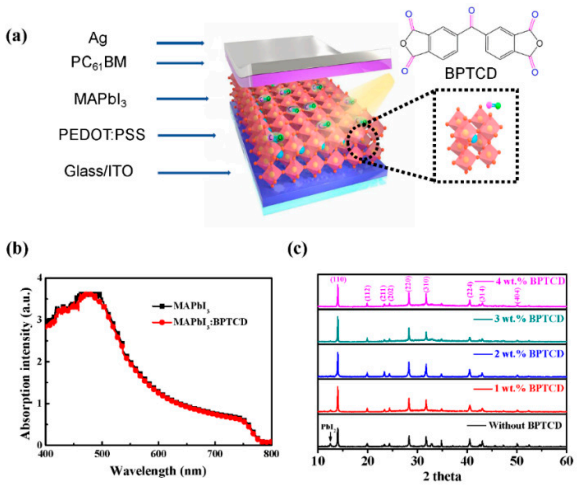

Figure 1. (**a**) A schematic diagram of the exploded view of PePDs. The dotted box shows the molecular structures of $MAPbI_3$ and BPTCD. (**b**) Absorption spectra of the perovskite films with and without BPTCD additive (**c**) XRD patterns of the perovskite film with different concentrations of BPTCD additive.

Additionally, the pure perovskite film exhibits a weak diffraction peak at 12.5°, which corresponds to the (001) plane of unconverted PbI_2. The existence of PbI_2 is typically due to the inefficient reaction between the PbI_2 and MAI precursor or decomposition of $MAPbI_3$ induced by ambient exposure [37–39]. Owing to the passivation function of the PbI_2, PbI_2 residues in the perovskite film could lower the opportunities of charge carrier recombination, thus lead to an improved photocurrent (I_{ph}) and EQE of PePDs [16,38].

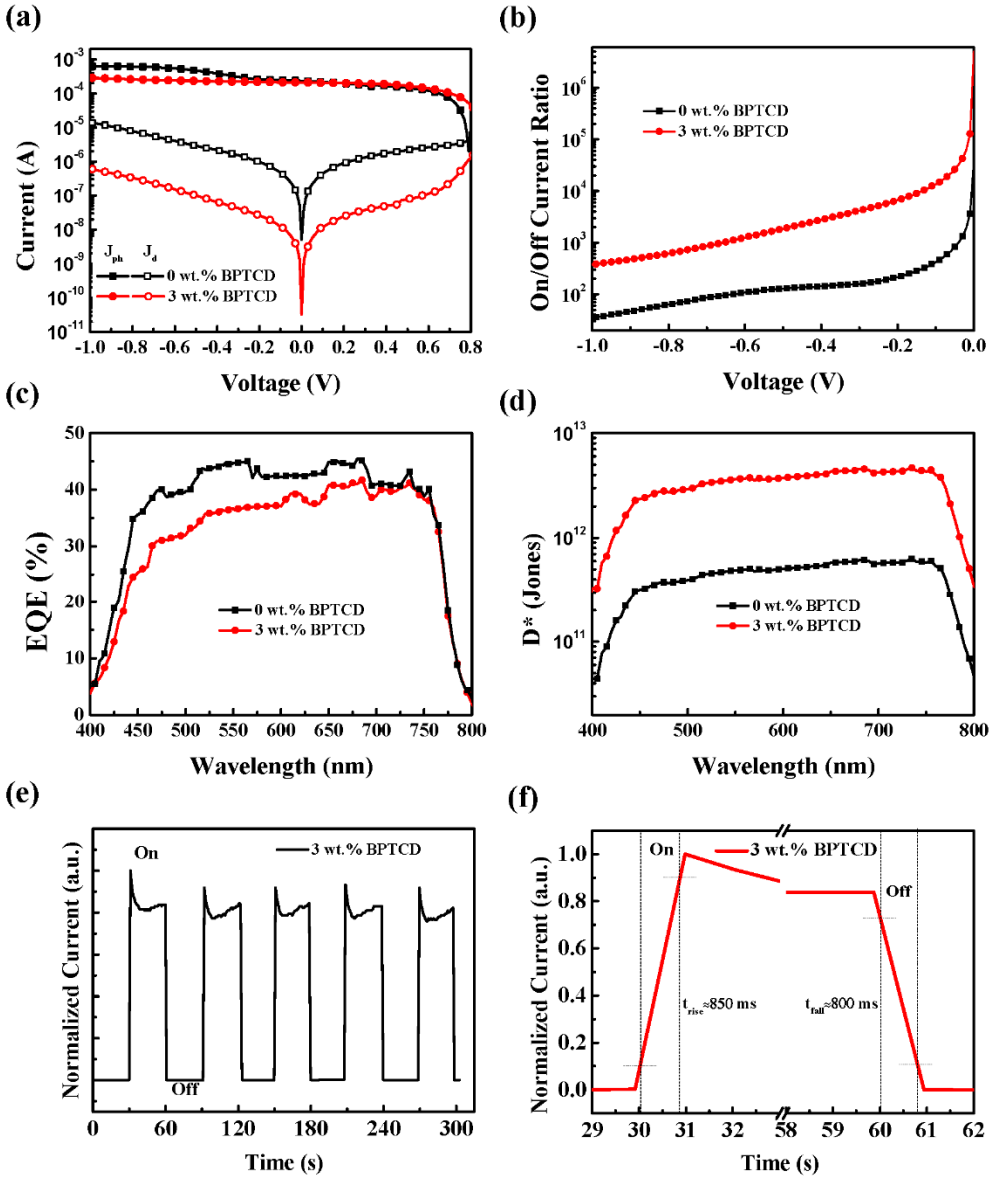

Figure 2. Electrical properties of PePDs with pure perovskite film and 3 wt.% BPTCD added perovskite film. (**a**) Semi-log I-V characteristics under light and dark condition; (**b**) On/off current ration; (**c**) Measured EQE spectra and (**d**) calculated D* values at −0.1 V; (**e**) Dynamic photo response measurements of PePDs with 3 wt.% BPTCD by multiple cycles introducing and removal white light (intensity of 100 mW/cm^2); (**f**) Temporal photo-response of the PePDs with 3 wt.% BPTCD.

To demonstrate the effect of the BPTCD additive upon device performances, the I_{ph} and I_d of PePDs were tested under white light irradiation and dark condition, respectively. The semi-log I-V characteristics of these PePDs are shown in Figure 2a and Figure S1. Typically, a low I_d is a key factor for high performance PePDs [12,13,16,40]. Here the control device with pure perovskite film shows a high I_d value of 2.93×10^{-6} A at −0.5 V, while the I_d for those PePDs with BPTCD additive reveal much

lower values. The PePDs with 1, 2, 3 and 4 wt.% BPTCD show I_d values of 6.73×10^{-8} A, 1.06×10^{-7} A, 9.98×10^{-8} A and 7.06×10^{-8} A at −0.5 V, respectively. Nevertheless, the I_{ph} of the control device is slightly higher than that of the BPTCD added devices. The control device exhibits an I_{ph} of 4.74×10^{-4} A at −0.5 V while the I_{ph} of the devices with 1−4 wt% BPTCD additive are 8.75×10^{-5} A, 1.78×10^{-4} A, 2.33×10^{-4} A and 5.63×10^{-5} A at −0.5 V respectively. Since the most important parameter for PePDs is D*, which is taken into account the contribution from both photocurrent (on current) and dark current (off current). The on/off current ratio of the devices is studied as shown in Figure 2b and Figure S1b. It can be seen that BPTCD added devices have much higher on/off current ratio (over 10^3 at −0.5 V) than the control device. In addition, when the concentration of BPTCD additive increases to 4 wt.%, the on/off current ratio decreases significantly. Although the device with 4 wt.% BPTCD additive shows a relatively low I_d, its I_{ph} is much lower than other devices as well.

To further investigate the effect of the different concentration of BTPCD additives on photo-gain, the EQEs of the PePDs were calculated and analyzed. As displayed in Figure 2c and Figure S1, the control device shows a relatively higher EQE value exceeding 40 % in the Visible region, which is benefited from a better device performance under light condition proved by the above results of I–V characteristics. The BPTCD added devices also exhibit efficient photo response in the Visible region. The EQE values of devices slightly increase with the increase of BPTCD concentration from 1 wt.% to 3 wt.%, and then decrease when the concentration is enhanced to 4 wt.%. Furthermore, according to the EQE spectra of the PePDs, we can estimate the D* of the devices over the Visible region based on the equations as follows:

$$R = EQE \times \frac{q\lambda}{hc} \tag{1}$$

$$D^* = \frac{R}{2(qJ_d)^{\frac{1}{2}}} = EQE \times \frac{\lambda}{1240(2qJ_d)^{1/2}} \tag{2}$$

where c is the speed of light in a vacuum, q is the elementary charge of the electron. The calculated D* results at a bias of −0.1 V are shown in Figure 2d and Figure S1. Apparently, compared to the control device, the BPTCD added devices exhibit overwhelming D* values exceeding 10^{12} Jones over the entire Visible region. In particular, the device with 3 wt.% BPTCD additive achieves the highest D* value of 4.55×10^{12} Jones at a wavelength of 685 nm, where the enhancement of D* is attributed to the suppressed of I_d. In addition, the photo response of the white light in PePDs with 3 wt.% BPTCD as a function of time was measured and shown in Figure 2e. The photocurrent of these devices is consistent and repeatable, which indicated good stability of the device. The spike liked cure of the initial part of on current is due to the time precision limit of our test equipment. Meanwhile, the temporal photo-response of the PePDs with 3 wt.% BTPCD was also measured (Figure 2f). The rise and fall times are defined as the times for the transient current rising from 10% to 90% and decreasing from 90% to 10% of the maximum output current, respectively. The rise and fall times for the PePD with 3 wt.% BPTCD were approximately 850 ms and 800 ms, respectively, which was the detection limit of our equipment. The overall device performance of our PePDs with BPTCD and comparison with recent reported PePDs are summarized in Tables 1 and 2.

Table 1. Summarization of the I_d, I_{ph} and on/off ratio of the PePDs at −0.5 V, and D* at 685 nm.

BPTCD	I_d (A)	I_{ph} (A)	On/Off Ratio	D* (Jones) @−0.1 V
Without BPTCD	2.93×10^{-6}	4.74×10^{-4}	0.12×10^3	6.14×10^{11}
1 wt.% BPTCD	6.73×10^{-8}	8.75×10^{-5}	1.20×10^3	3.52×10^{12}
2 wt.% BPTCD	1.06×10^{-7}	1.78×10^{-4}	1.29×10^3	3.35×10^{12}
3 wt.% BPTCD	9.98×10^{-8}	2.33×10^{-4}	1.86×10^3	4.55×10^{12}
4 wt.% BPTCD	7.06×10^{-8}	5.63×10^{-5}	0.63×10^3	2.84×10^{12}

Table 2. Performance summary of reported perovskite-based photodetectors.

Materials	Detectivity (Jones)	EQE (%)	On/Off Ratio	Response Time	Ref.
Single-crystal $CsPbBr_3$	6.2×10^{10}@540 nm	-	1.5×10^3	2.96 ms	[18]
Single-crystal $MAPbBr_3$,	10^{10} in visible	-	10^4	150 μs	[41]
$MAPbI_3$	10^{12} in visible	80@ −0.1 V	-	280 ns	[22]
$MAPbI_3$: PbS QD	10^{12} in visible, 10^{11} in NIR	38@ 0 V	10^3	<500 ms	[13]
$MAPbI_3$: BPTCD	4.5×10^{12} in visible	42@ 0 V	10^3	≈800 ms	This work

To disclose the reason for the suppressed I_d in BPTCD added devices, the morphology of perovskite films with various concentrations of BPTCD additives was characterized by SEM (Figure 3 and Figure S2). The pure perovskite film exhibits a relatively poor morphology with uneven grain sizes and many interior pinholes. These defects of the pure perovskite film can lead to a high leak current of the PePDs under the dark condition [33,37], which is also proved by I-V curve shown in Figure 2. After introducing BPTCD additive, the morphology of perovskite film changes significantly: the grain sizes become smaller and much more compact, thus resulting in a dense perovskite film. More significantly, the 4 wt.% BPTCD added perovskite film exhibits the smallest perovskite grain size, and the highest film coverage ratio. The improvement of film density can reduce the leak current of the devices, responsible for a suppressed I_d. Atomic force microscopy (AFM) was also employed to study the morphology of perovskite films. As displayed in Figure S3, the perovskite film with 3 wt.% BPTCD shows smaller grain size and smoother surface than the pure perovskite. Larger grain size of pure perovskite film may lead to larger undulation thus rougher surface than perovskite film with 3 wt.% BPTCD. Benefited from smooth surface of perovskite film with 3 wt.% BPTCD, the contact interface property between perovskite film and PCBM film can be improved to suppress the leak current, resulting in low dark current. However, as shown in Figure S1, photocurrents of the devices with BPTCD additives decrease. Especially in the case of 4% BPTCD, the photocurrent is decrease by nearly one order compared to the control device. This phenomenon could be attributed to the decrease of grain size of $MAPbI_3$ microstructure that would also lower the performance of the PePDs under light irradiation by unexpected loss of photo-induced charge carriers [39]. Benefited from the small-sized perovskite grains for 4 wt.% BPTCD added device, I_d decreased obviously, however, the I_{ph} also decreases, thus cause a performance deterioration. Therefore, a scrupulous balance between the grain size and film density should be considered for achieving high performance PePDs.

To illuminate the molecular interaction between BPTCD and PbI_2, FTIR measurement was employed. As reported by Bi et al. [38], the C=O group can interact with PbI_2 and trigger heterogeneous nucleation of $MAPbI_3$, thus improve the crystallinity of the perovskite film. Similar results were also reported by Peng et al. [42], such that the C=O groups are responsible for the passivation of perovskite film via Lewis-base electronic passivation of Pb^{2+} ions, which reduces trap density and enhances the morphology of perovskite film. Here the used BPTCD as an additive is rich of C=O groups, which may share the similar effect on the improvement of perovskite film quality. As displayed in Figure 4a, the stretching vibration of C=O groups in the pure BPTCD shows at 1749 cm^{-1}, while it shifts to 1743 cm^{-1} with the addition of PbI_2. This result indicates a weakening of the C=O bond derived from molecular interaction between BPTCD and the PbI_2 precursor, which is consistent with the previous reports [38,42]. The weakening of the C=O bond is indicative of the formation of an intermediate BPTCD-PbI_2 adduct, which can be expected to improve the crystallinity of the perovskite film [38,43]. Therefore, in this work, the BPTCD additive plays a role to favor the heterogeneous nucleation of the $MAPbI_3$, lower the energy barrier of nucleation and consequently to generate a high density of nuclei, leading to a more compact and smaller sized $MAPbI_3$ microstructure [38,43,44].

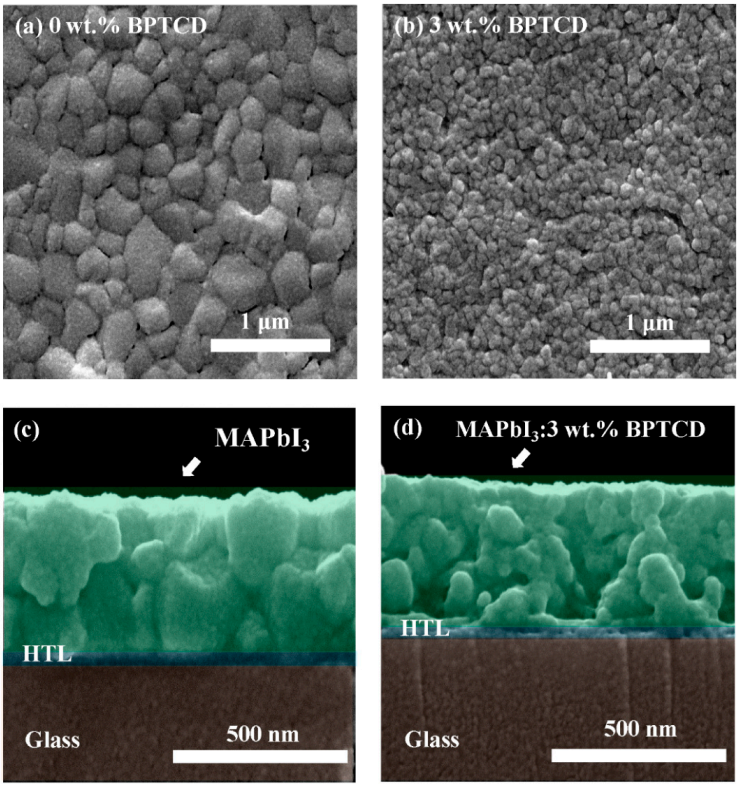

Figure 3. Top SEM images of perovskite films with (**a**) 0 and (**b**) 3 wt.% BPTCD additives. Cross SEM images of perovskite films with (**c**) 0 and (**d**) 3 wt.% BPTCD additives.

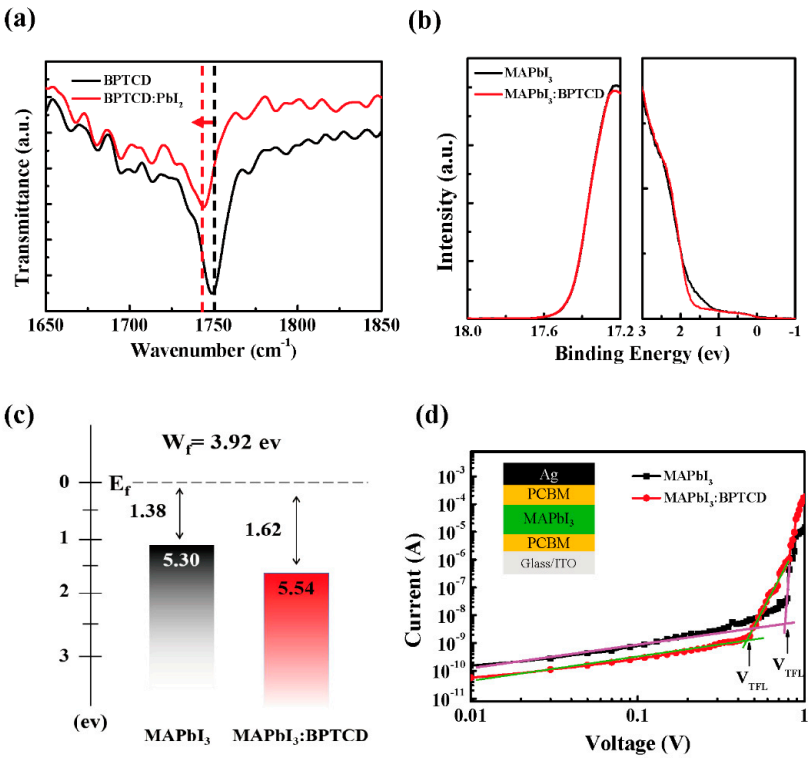

Figure 4. (**a**) FTIR spectra of pure BPTCD film and PbI_2 added BPTCD film (**b**) UPS results and (**c**) Energy level diagram of perovskite films with 3 wt.% and without BPTCD additive (**d**) I-V characteristic of an electron-only device based on perovskite film with 3 wt.% BPTCD, with an inset showing the device structure.

The interfacial properties in the photodetectors dominate the charge extraction and transportation, thus influence the performance of PePDs [37]. Here, the UPS measurement (with a He I of 21.2 eV) of perovskite films on the ITO substrates was carried out to characterize the change of energy levels of the perovskite films with and without BPTCD additive (Figure 4b). The high binding energy cutoff region is shown in the left panel, while the onset region is in the right panel. The perovskite films with and without BPTCD additive share nearly the same high binding energy cutoff and the work function is estimated to be 3.92 eV. However, the valence band minimum (VBM) position of the pure perovskite film occurs at 1.38 eV below Femi level (E_f) while the VBM position of perovskite film with BPTCD additive shifts to 1.62 eV below E_f, indicating a deeper VBM energy level (Figure 4c). This energy shift could lead to a mismatch of energy levels between the perovskite film and PEDOT:PSS (HOMO of 4.9 eV), which hinders the hole injection into the active layer due to the energy barrier and therefore suppress the I_d. However, this unmatched energy level could lead to the suppress of I_{ph} as well.

To study the influence of the trap density in the perovskite film on the dark current, the electron-only devices (ITO/PCBM/$MAPbI_3$/PCBM/Ag) were fabricated to analyze the trap density by using the space charge limited current (SCLC) method. The I-V curves of the devices with and without the BPTCD additive are shown in Figure 4d. The linear I-V plot indicates an Ohmic response at low bias, and the current increase nonlinearly when the bias voltage exceeds the trap-filled limit voltage (V_{TFL}), demonstrating that all the available trap states are filled by the injected charge carriers [45]. The onset voltage V_{TFL} is linearly proportional to the density of trap states η_t, which follows as Equation (3):

$$V_{TFL} = e\eta_t L^2/2\varepsilon\varepsilon_0 \quad (3)$$

where e is the elementary charge of the electron ($e = 1.6 \times 10^{-19}$ C), L is the perovskite film thickness, ε is the relative dielectric constant of $MAPbI_3$ (here we use 32 [45]), ε_0 is the vacuum permittivity ($\varepsilon_0 = 8.854 \times 10^{-12}$ F/m), and η_t is the trap state density of perovskite film. The V_{TFL} of the $MAPbI_3$ film with and without BPTCD additive can be identified in Figure 4d, respectively. The thickness of perovskite film with and without BPTCD additive is 431 nm and 397 nm, respectively, derived from the cross-section SEM images in Figure 3c,d. The electron trap state density of perovskite film with BPTCD additive is estimated as 1.01×10^{16} cm^{-3}, which is much lower than the perovskite film without BPTCD additive (1.50×10^{16} cm^{-3}). This decrease of trap density is due to the Lewis-base nature of the oxygen atoms in the C=O groups on BPTCD, and Lewis base material can passivate the defects induced by Pb^{2+} as the recombination centers on the surface and grain boundaries of perovskite films [42]. Therefore, dark leakage current originated from defect could be significantly lowered by the passivation of BPTCD additive.

To further investigate the influence of BPTCD additive on the electrical properties of PePDs, the impedance of the devices was measured by an impedance analyzer under dark condition. The measured electrical parameters of R_1, R_2, R_3, C_1, CPE_1-T and CPE_1-P are listed in Table 3 through the fitting curves. In this circuit model (Figure 5a inset), the R_1, R_2, and R_3 correspond to the device series resistance, the interfacial resistance, and recombination resistance, respectively [37]. From the corresponding Nyquist plots, the R_1 of the pristine and BPTCD added PePDs are similar. The R_2 of BPTCD added devices is about two folds larger than that of the pristine devices. This result accounts for the great reduction of the leak current of BPTCD added devices [40,46,47] as depicted in the I-V curves in Figure 2a. The compact morphology, low trap density and relativity unmatched energy level between the active layer and PEDOT:PSS layer are responsible for the enhancement of R_2. Meanwhile, a minor decrease of R_3 in the control device is observed, which suggests that the pristine perovskite film with larger grain size can suppress charge recombination more effectively under light condition, resulting in a higher EQE and I_{ph} of the control device [48].

Table 3. Parameters of the equivalent circuit for PePDs with and without BPTCD additive.

Device	R_1 (Ω)	R_2 (kΩ)	R_3(kΩ)	C_1 (F)	CPE_1-T (F/c^2)	CPE_1-P
Without BPTCD	28.4	57.2	1.5	2.18×10^{-9}	2.07×10^{-9}	0.91
With BPTCD	26.9	111.7	1.7	2.36×10^{-9}	2.23×10^{-9}	0.95

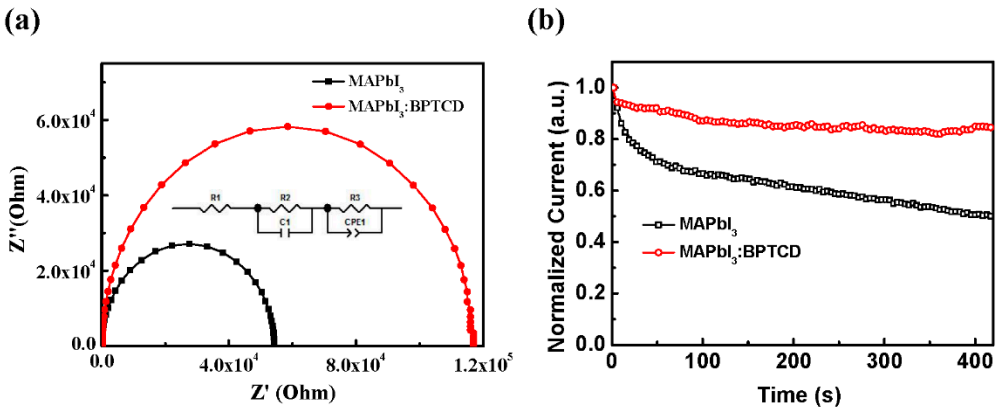

Figure 5. (**a**) Impedance spectra of PePDs, inset shows the corresponding equivalent circuit; (**b**) Long-term I_{ph} measurement of PePDs with and without BPTCD (under 100 mW/m^2 white light).

Finally, to examine the contribution of BPTCD additive toward the stability of PePDs, we performed a long-term photocurrent measurement on the PePDs with and without BPTCD additive. As shown in Figure 5b, the I_{ph} of the PePD with BPTCD additive can maintain 85% of the original value after operating 400 s, while the control device only maintains 47% I_{ph}. The enhancement of device stability is attributed to the high-quality perovskite film with decreased defects, since the defects at grain boundaries typical provide charge accumulation sites and infiltration pathways for water vapor in air [49]. This is responsible for the irreversible moisture-induced degradation of perovskite, thus degrades the long-term stability of the devices. As mentioned above, the perovskite film with BPTCD shows much lower tarp density than the pristine perovskite film, indicating more stable crystal structure and enhanced long-term stability of PePDs.

4. Conclusions

In summary, we developed a simple route for controlling the microstructure of $MAPbI_3$ by using BPTCD as an additive, and realized high performance PePDs based on the well controlled $MAPbI_3$ film. The results showed that the interaction between C=O groups in BPTCD and the PbI_2 in perovskite precursors could favor the heterogeneous nucleation of the $MAPbI_3$, thus lower the energy barrier of nucleation and facilitate the growth of $MAPbI_3$ crystal structures. Moreover, the BPTCD additive could down-shift the VBM level of the perovskite film and therefore contributes to the reduction of I_d. As a result, the I_d of the devices was significantly suppressed by nearly two orders of magnitude compared to the control device but kept I_{ph} almost unchanged. Hence, with an optimal concentration of BPTCD additive (3 wt.%), the PePD exhibits a high D* value exceeding 10^{12} Jones over the Visible region with a maximum D* value of 4.55×10^{12} Jones at 685 nm at a bias of −0.1 V. Moreover, the PePDs with 3 wt.% BPTCD shows much greater stability comparing to the control devices. This work demonstrates a facile and low-cost method for tuning the $MAPbI_3$ microstructure to obtain high quality perovskite film and open a novel route to realize high performance PePDs.

Supplementary Materials: The following are available online at http://www.mdpi.com/2072-666X/11/12/1090/s1, Figure S1: (a) Semilog J-V characteristics, (b) On/off current radio (c) Measured EQE spectra and (d) Calculated D* values at −0.1 V of PePDs with various concentrations of BPTCD additive (e) Calculated responsivity values −0.1 V of PePDs with various concentrations of BPTCD additive., Figure S2: SEM images of perovskite film with different concentrations of BPTCD additive, Figure S3: AFM measurement of perovskite films with 3% BPTCD and without BPTCD.

Author Contributions: Conceptualization, Z.G. and Y.Z.; methodology, Z.G. and G.Y.; Investigation: Z.G. and G.H.; writing-original draft preparation, Z.G.; writing-review and editing, J.Y., X.Y.; supervision, J.Y., X.Y.; project administration, J.Y., X.Y.; funding acquisition, J.Y., X.Y. All authors have read and agreed to the published version of the manuscript.

Funding: This work was financially supported by the National Key R&D Program of China (Grant No. 2018YFB0407102), the Foundation of National Natural Science Foundation of China (NSFC) (Grant Nos. 61421002, 61675041 & 51703019), Sichuan Science and Technology Program (Grant Nos. 2019YFH0005, 2019YFG0121, and 2019YJ0178, 2020YFH0181), and City University of Hong Kong (Grant No. 9610423, 9667199).

Acknowledgments: This work is also sponsored by Sichuan Province Key Laboratory of Display Science and Technology.

Conflicts of Interest: The authors declare no conflict of interest.

References

1. Yang, W.; Noh, H.; Jeon, N.; Kim, Y.; Ryu, S.; Seo, J.; Seok, S. High-performance photovoltaic perovskite flayers fabricated through intramolecular exchange. *Science* **2015**, *348*, 1234–1237. [CrossRef] [PubMed]
2. Lee, M.; Teuscher, J.; Miyasaka, T.; Murakami, N.; Snaith, H.J. Efficient hybrid solar cells based on meso-superstructured organometal halide perovskites. *Science* **2012**, *338*, 643–647. [CrossRef] [PubMed]
3. Zheng, Y.; Kong, J.; Huang, D.; Shi, W.; McMillon-Brown, L.; Katz, H.E.; Yu, J.; Taylor, A.D. Spray coating of the PCBM electron transport layer significantly improves the efficiency of p-i-n planar perovskite solar cells. *Nanoscale* **2018**, *10*, 11342–11348. [CrossRef] [PubMed]
4. Zheng, Y.; Shi, W.; Kong, J.; Huang, D.; Katz, H.E.; Yu, J.; Taylor, A.D. A Cytop insulating tunneling layer for efficient perovskite solar cells. *Small Methods* **2017**, *1*, 11700244. [CrossRef]
5. Wang, N.; Cheng, L.; Ge, R.; Zhang, S.; Miao, Y.; Zou, W.; Yi, C.; Sun, Y.; Cao, Y.; Yang, R.; et al. Huang. Perovskite light-emitting diodes based on solution-processed self-organized multiple quantum wells. *Nat. Photonics* **2016**, *10*, 699–704. [CrossRef]
6. Shi, Y.; Wu, W.; Dong, H.; Li, G.; Xi, K.; Divitini, G.; Ran, C.; Yuan, F.; Zhang, M.; Jiao, B.; et al. A strategy for architecture design of crystalline perovskite light-emitting diodes with high performance. *Adv. Mater.* **2018**, *30*, 1800251. [CrossRef]
7. Wang, Z.; Li, Z.; Zhou, D.; Yu, J. Low turn-on voltage perovskite light-emitting diodes with methanol treated PEDOT:PSS as hole transport layer. *Appl. Phys. Lett.* **2017**, *111*, 233304. [CrossRef]
8. Xing, G.; Mathews, N.; Lim, S.S.; Yantara, N.; Liu, X.; Sabba, D.; Gratzel, M.; Mhaisalkar, S.; Sum, T.C. Low-temperature solution-processed wavelength-tunable perovskites for lasing. *Nat. Mater.* **2014**, *13*, 476–480. [CrossRef]
9. Wang, K.; Sun, W.; Li, J.; Gu, Z.; Xiao, S.; Song, Q. Unidirectional lasing emissions from $CH_3NH_3PbBr_3$ perovskite microdisks. *ACS Photonics* **2016**, *3*, 1125–1130. [CrossRef]
10. Gu, Z.; Wang, K.; Sun, W.; Li, J.; Liu, S.; Song, Q.; Xiao, S. Two-photon pumped $CH_3NH_3PbBr_3$ perovskite microwire lasers. *Adv. Opt. Mater.* **2016**, *4*, 472–479. [CrossRef]
11. Hu, X.; Zhang, X.; Liang, L.; Bao, J.; Li, S.; Yang, W.; Xie, Y. High-performance flexible broadband photodetector based on organolead halide perovskite. *Adv. Funct. Mater.* **2014**, *24*, 7373–7380. [CrossRef]
12. Dou, L.; Yang, Y.M.; You, J.; Hong, Z.; Chang, W.H.; Li, G.; Yang, Y. Solution-processed hybrid perovskite photodetectors with high detectivity. *Nat. Commun.* **2014**, *5*, 5404. [CrossRef] [PubMed]
13. Zhao, D.; Huang, J.; Qin, R.; Yang, G.; Yu, J. Efficient visible-near-infrared hybrid perovskite:pbs quantum dot photodetectors fabricated using an antisolvent additive solution process. *Adv. Opt. Mater.* **2018**, *6*, 1800979. [CrossRef]
14. Xie, C.; Yan, F. Enhanced performance of perovskite/organic-semiconductor hybrid heterojunction photodetectors with the electron trapping effects. *J. Mater. Chem. C* **2018**, *6*, 1338–1342. [CrossRef]
15. Wang, Y.; Yang, D.; Zhou, X.; Alshehri, S.M.; Ahamad, T.; Vadim, A.; Ma, D. Vapour-assisted multi-functional perovskite thin films for solar cells and photodetectors. *J. Mater. Chem. C* **2016**, *4*, 7415–7419. [CrossRef]

16. Wang, H.; Haroldson, R.; Balachandran, B.; Zakhidov, A.; Sohal, S.; Chan, J.Y.; Zakhidov, A.; Hu, W. Nanoimprinted perovskite nanograting photodetector with improved efficiency. *ACS Nano* **2016**, *10*, 10921–10928. [CrossRef]
17. Chun, D.H.; Choi, Y.J.; In, Y.; Nam, J.K.; Choi, Y.J.; Yun, S.; Kim, W.; Choi, D.; Kim, D.; Shin, H.; et al. Halide perovskite nanopillar photodetector. *ACS Nano* **2018**, *12*, 8564–8571. [CrossRef]
18. Zhang, Y.; Li, S.; Yang, W.; Joshi, M.; Fang, X. Millimeter-sized single-crystal $CsPbBr_3$/CuI heterojunction for high-performance self-powered photodetector. *J. Phys. Chem. Lett.* **2019**, *10*, 2400–2407. [CrossRef]
19. Lin, C.H.; Cheng, B.; Li, T.Y.; Retamal, J.; Wei, T.C.; Fu, H.C.; Fang, X.; He, J.H. Orthogonal lithography for halide perovskite optoelectronic nanodevices. *ACS Nano* **2019**, *13*, 1168–1176. [CrossRef]
20. AlAmri, A.M.; Leung, S.F.; Vaseem, M.; Shamim, A.; He, J.H. Fully inkjet-printed photodetector using a graphene/perovskite/graphene heterostructure. *IEEE. Trans. Electron. Dev.* **2019**, *6*, 66. [CrossRef]
21. Chen, L.; Cai, J.; Li, J.; Feng, S.; Wei, G.; Li, W. Nanostructured texturing of $CH_3NH_3PbI_3$ perovskite thin film on flexible substrate for photodetector application. *Org. Electron.* **2019**, *71*, 284–289. [CrossRef]
22. Fang, Y.; Huang, J. Resolving weak light of sub-picowatt per square centimeter by hybrid perovskite photodetectors enabled by noise reduction. *Adv. Mater.* **2015**, *27*, 2804–2810. [CrossRef] [PubMed]
23. Tang, F.; Chen, Q.; Chen, L.; Ye, F.; Cai, J.; Chen, L. Mixture interlayer for high performance organic-inorganic perovskite photodetectors. *Appl. Phys. Lett.* **2016**, *109*, 123301. [CrossRef]
24. Zhu, H.L.; Cheng, J.; Zhang, D.; Liang, C.; Reckmeier, C.J.; Huang, H.; Rogach, A.L.; Choy, W.C. Room-temperature solution-processed NiOx:PbI_2 nanocomposite structures for realizing high-performance perovskite photodetectors. *ACS Nano* **2016**, *10*, 6808–6815. [CrossRef]
25. Zhang, Y.; Xu, W.; Xu, X.; Cai, J.; Yang, W.; Fang, X. Self-powered dual-color UV-green photodetectors based on SnO_2 millimeter wire and microwires/$CsPbBr_3$ particle heterojunctions. *J. Phys. Chem. Lett.* **2019**, *10*, 836–841. [CrossRef]
26. Cai, S.; Xu, X.; Yang, W.; Chen, J.; Fang, X. Materials and designs for wearable photodetectors. *Adv. Mater.* **2019**, *31*, 1808138. [CrossRef]
27. Su, H.; Meng, L.; Liu, Y.; Zhang, Y.; Hu, M.; Yang, Z.; Liu, S. (Frank) Effective electron extraction from active layer for enhanced photodetection of photoconductive type detector with structure of Au/$CH_3NH_3PbI_3$/Au. *Org. Electron.* **2019**, *74*, 197–203. [CrossRef]
28. Li, J.; Yuan, S.; Tang, G.; Li, G.; Liu, D.; Li, J.; Hu, X.; Liu, Y.; Li, J.; Yang, Z.; et al. High-performance self-powered photodetectors based on perovskite and graphene. *ACS Appl. Mater. Interfaces* **2017**, *9*, 42779–42787. [CrossRef]
29. Yu, X.; Marks, T.J.; Facchetti, A. Metal oxides for optoelectronic applications. *Nat. Mater.* **2016**, *15*, 383–396. [CrossRef]
30. Ma, C.; Shi, Y.; Hu, W.; Chiu, M.H.; Liu, Z.; Bera, A.; Li, F.; Wang, H.L.; Li, J.; Wu, T. Heterostructured WS_2/$CH_3NH_3PbI_3$ photoconductors with suppressed dark current and enhanced photodetectivity. *Adv. Mater.* **2016**, *28*, 3683–3689. [CrossRef]
31. Maity, P.; Yin, J.; Cheng, B.; He, J.H.; Bakr, O.M.; Mohammed, O.F. Layer-dependent coherent acoustic phonons in two-dimensional ruddlesden-popper perovskite crystals. *J. Phys. Chem. Lett.* **2019**, *10*, 5259–5264. [CrossRef] [PubMed]
32. Dong, Y.; Zou, Y.; Song, J.; Song, X.; Zeng, H. Recent progress of metal halide perovskite photodetectors. *J. Mater. Chem. C* **2017**, *5*, 11369–11394. [CrossRef]
33. Ahmadi, M.; Wu, T.; Hu, B. A Review on organic-inorganic halide perovskite photodetectors: Device engineering and fundamental physics. *Adv. Mater.* **2017**, *29*, 922–930. [CrossRef] [PubMed]
34. Shekargoftar, M.; Jurmanová, J.; Homola, T. A study on the effect of ambient air plasma treatment on the properties of methylammonium lead halide perovskite films. *Metals* **2019**, *9*, 991. [CrossRef]
35. Valastro, S.; Smecca, E.; Sanzaro, S.; Giannazzo, F.; Deretzis, I.; Magna, A.; Numata, Y.; Jena, A.; Miyasaka, T.; Gagliano, A.; et al. Improved electrical and structural stability in htl-free perovskite solar cells by vacuum curing treatment. *Energies* **2020**, *13*, 3953. [CrossRef]
36. Yu, J.; Chen, X.; Wang, Y.; Zhou, H.; Xue, M.; Xu, Y.; Li, Z.; Ye, C.; Zhang, J.; Aken, P.A.; et al. A high-performance self-powered broadband photodetector based on a $CH_3NH_3PbI_3$ perovskite/ZnO nanorod array heterostructure. *J. Mater. Chem. C* **2016**, *4*, 7302–7308. [CrossRef]

37. Fan, P.; Zheng, D.; Zheng, Y.; Yu, J. Efficient and stable planar p-i-n perovskite solar cells by doping tungsten compound into PEDOT:PSS to facilitate perovskite crystalline. *Electrochim. Acta* **2018**, *283*, 922–930. [CrossRef]
38. Bi, D.; Yi, C.; Luo, J.; Décoppet, J.-D.; Zhang, F.; Zakeeruddin, S.M.; Li, X.; Hagfeldt, A.; Grätzel, M. Polymer-templated nucleation and crystal growth of perovskite films for solar cells with efficiency greater than 21%. *Nat. Energy* **2016**, *1*, 16142. [CrossRef]
39. Zheng, D.; Yang, G.; Zheng, Y.; Fan, P.; Ji, R.; Huang, J.; Zhang, W.; Yu, J. Carbon nano-onions as a functional dopant to modify hole transporting layers for improving stability and performance of planar perovskite solar cells. *Electrochim. Acta* **2017**, *247*, 548–557. [CrossRef]
40. Wang, H.; Zheng, Y.; Qin, R.; Yu, J. Highly sensitive panchromatic ternary polymer photodetectors enabled by Förster resonance energy transfer and post solvent treatment. *J. Phys. D Appl. Phys.* **2018**, *51*, 104002. [CrossRef]
41. Shaikh, P.A.; Shi, D.; Retamal, J.R.D.; Sheikh, A.D.; Haque, M.; Kang, C.; He, J.H.; Bakr, O.M.; Wu, T. Schottky junctions on perovskite single crystals: Light-modulated dielectric constant and self-biased photodetection. *J. Mater. Chem. C* **2016**, *4*, 8304–8312. [CrossRef]
42. Peng, J.; Khan, J.I.; Liu, W.; Ugur, E.; Duong, T.; Wu, Y.; Shen, H.; Wang, K.; Dang, H.; Aydin, E.; et al. A universal double-side passivation for high open-circuit voltage in perovskite solar cells: Role of carbonyl groups in poly(methyl methacrylate). *Adv. Energy Mater.* **2018**, *8*, 1801208. [CrossRef]
43. Lee, J.W.; Kim, H.S.; Park, N.G. Lewis acid-base adduct approach for high efficiency perovskite solar cells. *Acc. Chem. Res.* **2016**, *49*, 311–319. [CrossRef] [PubMed]
44. Gao, Z.; Zheng, Y.; Zhao, D.; Yu, J. Spin-coated $CH_3NH_3PbBr_3$ film consisting of micron-scale single crystals assisted with a benzophenone crystallizing agent and its application in perovskite light-emitting diodes. *Nanomaterials* **2018**, *8*, 787. [CrossRef] [PubMed]
45. Dong, Q.; Fang, Y.; Shao, Y.; Mulligan, P.; Qiu, J.; Cao, L.; Huang, J. Electron-hole diffusion lengths > 175 mum in solution-grown $CH_3NH_3PbI_3$ single crystals. *Science* **2015**, *347*, 967–970. [CrossRef]
46. Zheng, Y.; Goh, T.; Fan, P.; Shi, W.; Yu, J.; Taylor, A.D. Toward efficient thick active PTB7 photovoltaic layers using diphenyl ether as a solvent additive. *ACS Appl. Mater. Interfaces* **2016**, *8*, 15724–15731. [CrossRef]
47. Leem, D.-S.; Lee, K.-H.; Kwon, Y.-N.; Yun, D.-J.; Park, K.-B.; Lim, S.-J.; Kim, K.-S.; Jin, Y.W.; Lee, S. Low dark current inverted organic photodetectors employing MoOx:Al cathode interlayer. *Org. Electron.* **2015**, *24*, 176–181. [CrossRef]
48. Huang, P.; Liu, Y.; Zhang, K.; Yuan, L.; Li, D.; Hou, G.; Dong, B.; Zhou, Y.; Song, B.; Li, Y. Catechol derivatives as dopants in PEDOT:PSS to improve the performance of p-i-n perovskite solar cells. *J. Mater. Chem. A* **2017**, *5*, 24275–24281. [CrossRef]
49. Ahn, N.; Kwak, K.; Jang, M.S.; Yoon, H.; Lee, B.Y.; Lee, J.K.; Pikhitsa, P.V.; Byun, J.; Choi, M. Trapped charge-driven degradation of perovskite solar cells. *Nat. Commun.* **2016**, *7*, 13422. [CrossRef]